F. Alonso-Marroquin · A.A. Peña · H. J. Herrmann and P. Mora

Simulation of shear bands using polygonal particles

Abstract The choice of particle shape representation is critical in the accuracy of the simulations of real granular materials. Here we present a method to simulate particle shape using polygonal particles. The method reproduces shear bands using different boundary conditions: confining walls, floppy boundaries and periodic boundary conditions.

Keywords grain shape · polygonal particles · shear bands

1 Introduction

One of the most remarkable features in granular media is the formation of shear bands: For large shear deformation strain is not homogeneously distributed but appears in a localized fashion along narrow interfaces between two unstrained bodies. Geological fault zones is a typical example of shear bands. They consist of layers of fragmented rocks, which are squeezed by the slow relative movement of the tectonic plates. The dynamics of the granular materials within such layers is thought to control earthquake instability, and thus understanding its properties is central to an understanding of the earthquake process [1].

In laboratory experiments shear bands turn out to be very sensitive the the boundary conditions. In Couette shear cells they are localized near the inner cylinder [2]. In wall-confined samples, shear bands emerge near any irregularity of the walls, They *reflect* when they reach a rigid boundary, and *refract* when enter to a granular medium with different bulk properties [3]. A recent review of experiments on strain localization

F. Alonso-Marroquin and P. Mora
Earth Systems Science Computational Centre,
The University of Queensland, Sta. Lucia, Qld. 4067 Australia
E-mail: fernando@esscc.uq.edu.au
A.A. Peña and H.J. Herrmann
Institute for Computational Physics,
University of Stuttgart, Pfaffenwaldring 27, 70569 Stuttgart, Germany E-mail: andres@icp.uni-stuttgart.de

states that *"depending on the boundary conditions various patterns of localization were observed, including parallel and crossing shear bands, as well as temporary, or 'non-persistent' modes of localization, that is,localized regions which form during the test and eventually 'disappear'".* [4]

Granular dynamics simulations has been used to model shear bands using different boundary conditions [5; 6; 7]. They provide detailed micromechanical data, which are not available in conventional laboratory experiments. Most models use disks or spheres to represent the particle shape. The simplicity of their geometry reduce the computer time, and allows to use foolproof contact force laws in the calculation of the interactions. However, these models does not take into account the diversity of shapes of the grains in realistic granular materials.

This paper presents a detailed review of the method that has been used to model granular materials using polygonal particles. We discuss also different boundary conditions leading to shear band formation. In Section 2 we introduce the Voronoi tessellation used to generate polygonal packings. The contact force model is presented in Section 3. The contact detection and speed up the numerical simulations is presented in Section 4. In Section 5 the implementation of boundary conditions and their implications in shear band formation is discussed.

2 Generation of polygons

The polygons representing the particles in this model are generated by using the method of Voronoi tessellation: First, a regular square lattice of side ℓ is created. Next, we set a random point in a square of side length a inside the cells of the rectangular grid. Then, each polygon is constructed, assigning to each point that part of the plane that is nearer to it than to any other point. The details of the construction of the Voronoi cells can be found in the literature [8; 9].

Fig. 1 shows random tessellations for different values of a. In all the cases, the mean number of edges is six
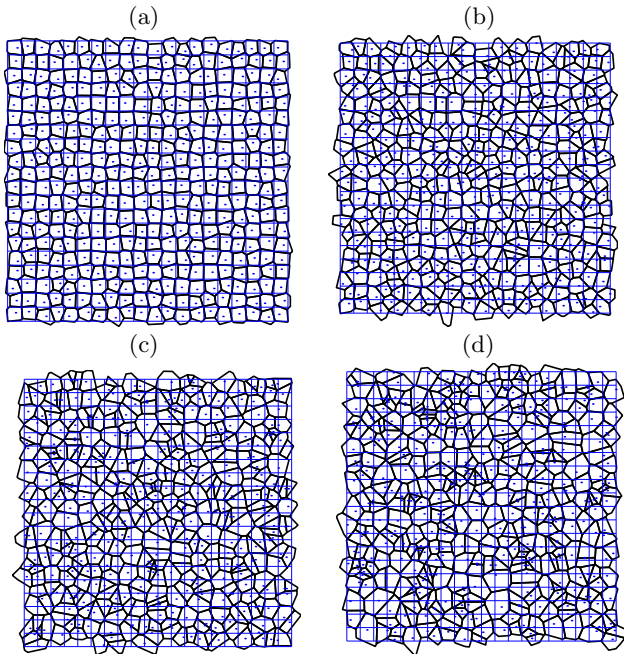
Fig. 1 Voronoi construction used to generate the convex polygons. The dots indicate the point used to the tessellation. Periodic boundary conditions were used. Four different values of a are chosen: 0.5ℓ, ℓ, 2ℓ and 20ℓ.

[9]. The tessellation with $a \leq \ell$ corresponds to the so-called *vectorizable random lattices* [8]. They are Voronoi constructions with low disorder, a narrow distribution of areas and a certain anisotropy when $a < \ell$ as shown in part (a) of Fig. 1. This anisotropy is reflected in the fact that the orientational distribution of the edges is not uniform. The tessellations with $a > \ell$ lead to isotropic Voronoi tessellations with a wide, asymmetric distributions of areas of the polygons (see parts (b) and (c) of Fig. 1). In particular, the limit $a \gg \ell$ corresponds to the so-called Poisson tessellations [8; 9].

Voronoi tessellations with $a = \ell$ will be used in this work. In this case, the orientational distribution of edges is isotropic, and the diversity of areas of polygons is symmetric around ℓ^2 [10]. These two properties are observed in realistic granular materials [11; 12]. The probabilistic distribution of areas follows approximately a Gaussian distribution with a variance of $0.36\ell^2$. the number of edges of the polygons is distributed between 4 and 8 for 98.7% of the polygons.

Initially, The polygonal particles fill the plane with no overlaps and no gaps. This kind of plain tessellation resembles in some aspects the geometry of fragmented rocks, dry masonry walls or marble [13]. It should recognized that this model is an oversimplification of such materials. However, this model allow us to investigate granular media in the extreme case of an initial space filling packings of angular particles, and compare the results with the other extreme case of perfect spherical particles with large initial porosity [13]. A method to generate packing fractions lower than one will be explained in Sec. 5.1.

3 Contact Forces

Defining contact forces between polygonal particles is far to be a trivial task. A usual approach is to assume that the polygons cannot be deformed, but they can overlap when they are pressed against each other. Then the force is calculated as a function of this overlap [14; 15]. For the calculation of the contact force we require two well defined quantities: contact normal vector and overlapping length. The first one is the vector perpendicular to the contact surface. The latter one is a measure the interpenetration between the two particles . It is desirable that these two quantities change continuously with time. Time discontinuities in the force eventually lead to numerical problems in the integration of the equation of motions, such as numerical generation of energy in the granular system.

The contact normal vector is taken perpendicular to the so-called *contact line*. This line represents the flattened contact surface between the two bodies in contact. We calculate the contact line from the intersection points of the overlapping polygons. In most cases, we have two intersection points, as shown in the left of Fig. 2. In such a case, the contact line is defined by the vector $\mathbf{C} = \overrightarrow{C_1C_2}$ connecting these two intersection points. In some pathological cases, the intersection of the polygons leads to four or six points. In these cases, we define the contact line by the vector $\mathbf{C} = \overrightarrow{C_1C_2} + \overrightarrow{C_3C_4}$ or $\mathbf{C} = \overrightarrow{C_1C_2} + \overrightarrow{C_3C_4} + \overrightarrow{C_5C_6}$, respectively. This choice guarantees a continuous change of the contact line, and therefore of the contact normal vector, during the evolution of the contact.

The contact force is separated as $\mathbf{f}^c = \mathbf{f}^e + \mathbf{f}^v$, where $\mathbf{f}^e$ and $\mathbf{f}^v$ are the elastic and viscous contribution. The elastic part of the contact force is decomposed as $\mathbf{f^e} = f_n^e \hat{n}^c + f_t^e \hat{t}^c$, where f_n^e is the normal elastic force and f_t^3 is the frictional force . The calculation of these components is explained below. The unit tangential vector is defined as $\hat{t}^c = \mathbf{C}/|\mathbf{C}|$, and the normal unit vector $\hat{n}^c$ is taken perpendicular to $\mathbf{C}$. The point of application of the contact force is taken as the center of mass of the overlapping polygon.

As opposed to the Hertz theory for round contacts, there is no exact way to calculate the normal force between interacting polygons. Tillemans and Herrmann [14] propose to to calculate this force as $f_n^e = -k_n A/L_c$ where k_n is the normal stiffness, A is the overlapping area and L_c is a characteristic length of the polygon pair. Our choice of L_c is $1/2(1/R_i + 1/R_j)$ where R_i and R_j are the radii of the circles of the same area as the polygons. This normalization is necessary to be consistent in the units

of force. Since the overlapping area changes continuously in time, the normal elastic force is continuous too.

The frictional force is calculated using an variation of the Cundall-Strack method [16]: An elastic force $f_t^e = -k_t \Delta x_t$ proportional to the elastic displacement is included at each contact. k_t is the tangential stiffness. In order to satisfy the sliding condition $|f_t^e| < \mu f_n^e$, The elastic displacement Δx_t is calculated as follows: When two particles come into contact we set $\Delta x_t = 0$. Then, at each time t, we guess a new value for the tangential elastic deformation as:

$$\Delta x_t^p(t) = \Delta x_t(t - \Delta t) + v_t^c \Delta t, \tag{1}$$

where v_t^c is the tangential component of the relative velocity at the contact:

$$\mathbf{v}^c = \mathbf{v}_i - \mathbf{v}_j + \mathbf{w}_i \times \mathbf{l}_i - \mathbf{w}_j \times \mathbf{l}_j. \tag{2}$$

$\mathbf{v}_i$ is the linear velocity and $\mathbf{w}_i$ is the angular velocity of the particles in contact. $\mathbf{l}_i$ is the so-called *branch vector*, which connects the center of mass of the particle to the center of mass of the overlapping polygon The predicted value of elastic deformation is corrected to satisfy the Coulomb sliding condition:

$$\Delta x_t(t) = sign(\Delta x_t^p(t)) \min(\frac{\mu k_n \Delta x_n(t)}{k_t}, |\Delta x_t^p|). \tag{3}$$

This frictional force reproduces the main features of the plastic deformation of soils, such as the plastic flow-rule [13], the stick-slip fluctuations [17; 18] and ratcheting [19]. The main drawback of this method is that it introduces an time integration error of $O(\Delta t^2)$. Improvement of the calculations of such frictional force will require higher order integration terms in Eq. 1.

Finally, we introduce a viscous force (Eq. 4), which is necessary to maintain the numerical stability of the method and to obtain a quick convergence to the equilibrium configuration.

$$\mathbf{F}_v^c = -m(\gamma_n \cdot \mathbf{v}_n^c \cdot \hat{n}^c - \gamma_t \cdot \mathbf{v}_t^c \cdot \hat{t}^c), \tag{4}$$

where $m = (1/m_i + 1/m_j)^{-1}$ is the effective mass of the two particles in contact, γ_n and γ_t are the damping coefficients. These forces introduce time dependent
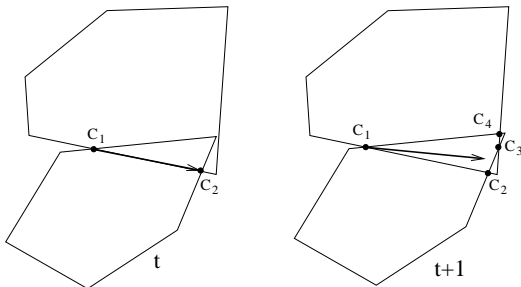

Fig. 2 Intersection points C_i before (left) and after the formation of a pathological contact (right). The vector denotes the contact line. t represents the time step.

effects during the loading. However, these effects can be arbitrarily reduced by increasing the loading time, as corresponds to the quasistatic approximation.

The transmitted torque between two polygons in contact is calculated as $\boldsymbol{\tau} = \boldsymbol{\ell} \times \mathbf{f}$. Since the point of application of the force is not collinear with the centers of masses of the interacting polygons, there is a contribution of the torque from both components of the contact force. This makes an important difference with respect to the interaction between disks or spheres: Polygons can transmit torques even in absence of frictional forces.

The evolution of the position $\mathbf{x}_i$ and the orientation φ_i of the polygon i is governed by the equations of motion:

$$m_i \ddot{\mathbf{x}}_i = \sum_c \mathbf{f_i^c} + \sum_b \mathbf{f}_i^b,$$
$$I_i \ddot{\varphi}_i = \sum_c \boldsymbol{\ell}_i^c \times \mathbf{f_i^c} + \sum_b \boldsymbol{\ell}_i^b \times \mathbf{f}_i^b. \tag{5}$$

Here m_i and I_i are the mass and moment of inertia of the polygon. The first sum goes over all those particles in contact with this polygon; the second one over all the forces applied on the boundary of the assembly. We use a fifth-order Gear predictor-corrector method for solving the equation of motion [20].

4 Neighbor search

The efficiency of the granular dynamics simulation is mainly determined by the method of contact detection. If the system consist of n particles, the required calculation operations for contact detection in each time step usually be $O(n^2)$. Special neighbor search algorithms such as Verlet lists and Link Cell Algorithms [21; 20] have been proposed to reduce the computational effort.

Our method combines Verlet Lists with a Link Cell algorithm to determine the list of particles in potential contact using $O(n)$ calculations. The Verlet list is nothing more than the list of pair particles which are relative close each other. We attach to each particle a *halo* of radius $R + \delta$, where R is the radius of a sphere containing the particle, and δ is the so-called *Verlet distance*. We call two particles *neighbors* if their halos overlap.

We use a Link Cell algorithm to allows a rapid calculation of this Verlet list: First, the space occupied by the particles is divided in cells of side $D + \delta$, where D is the maximal diameter of the polygons. Then the Link Cell List is defined as the list of particles hosted in each cell. Finally, the candidates of neighbors for each particle are searched only in the cell occupied by this particle, and its eight neighbor cells.

Of course, neighbor list do not need to be updated each time step. The list is kept constant until the maximal displacement of the particles after the last update

is larger than δ. Increasing the value of δ makes updating of the list less frequent, but it increases the size of this list, and hence, the ammount of memory used in the simulation. Therefore, the parameter δ must be chosen by making a compromise between the storage (size of the Vertex List) and the compute time (frequency of list updates).

There are many parameters in the molecular dynamics algorithm. The parameters k_n, k_t/k_n and μ can be considered as *material parameters*. They determine the constitutive response of the system in the quasistatic limit, so they should be adjusted to the experimental data [13]. we chose here $k_n = 1.6 \times 10^8 N/m$, $k_t = 0.33k_n$ and $\mu = 0.5$. The other parameters should be carefully chosen to preserve numerical stability, optimize the time of calculation and satisfy the quasistatic approximation.

5 Boundary Conditions

The presence of shear bands is very sensitive to the conditions imposed on the boundary of the granular assembly. In our simulations we have investigated three different boundary conditions. The first one corresponds to the confining walls. In the second case we mimic the experimental tests under plane strain conditions: First, a confining pressure is applied to the sample through a flexible membrane. Then, two horizontal walls at the top and bottom of the packing are used to apply vertical loading with constant velocity. Finally, we model infinitely large shear cells by introducing the periodic boundary condition along the horizontal direction.

5.1 Walls as boundaries

Usually, the granular assemblies are compacted and loaded within a set of confining walls. These walls act as boundary conditions, and can be moved by specifying their velocity or the force applied on them. The response of the walls can be used to calculate the global stress and strain of the assembly.

The interaction of the polygons with the walls is modeled here by using a simple visco-elastic force. First, we allow the polygons to penetrate the walls. Then, for each vertex of the polygon α inside of the walls we include a force

$$\mathbf{f}^b = -k_n \Delta x_n \mathbf{n} - \gamma_b m_\alpha \mathbf{v}^b, \tag{6}$$

where Δx_n is the penetration length of the vertex, $\mathbf{n}$ is the unit normal vector to the wall, and $\mathbf{v}^b$ is the relative velocity of the vertex with respect to the wall.

Confining walls can be used to generate samples with different void ratios. Starting from a very loose packing, the sample is compacted by applying a centripetal gravitational field to the particles and on the walls, oriented to the center of mass of the assembly. Then the sample

is subjected to an isotropic compression until the desired confining pressure is reached. In order to generate dense samples, the interparticle friction is set to zero during the construction. The loose samples are created taking damping coefficients 100 times greater than those used in the test stage. Samples with void ratio ranged from 0.128 to 0.271 can be achieved with this method [17].

We have investigated shear deformation of granular samples with different initial void ratios [17]. Shear bands are observed in dense samples, whereas they seems to be absent in loose ones. they share some common properties of the shear bands in real granular materials, such as their characteristic reflection when they reach the boundary wall. Shear band orientation lies between the Roscoe angle and Mohr-Coulomb solution, as in most of the experimental data.

For large shear deformations all samples reaches the critical state, which is independent on their initial density. Once the samples reaches this state, they deform at constant void ratio and coordination number [17]. The evolution of the deviatoric stress exhibits fluctuations around the residual strength. Abrupt reduction of the stress results from the collapse of force chains, as shown the Fig.3. collapse of force chains makes the sample to approach and retreats unstable stages. A similar behavior is observed in glass bead samples [22] and packings of glass spheres [23]. Experimental biaxial tests show evidence of *dynamic instabilities* at the critical state [24]. Erratic slip-stick motion at the critical state is interesting, owing to its potential analogy with earthquake dynamics [18].

5.2 Floppy boundary

The method of floppy boundary is introduced to model the typical biaxial test used to investigate the strain localization [11]. In this test, a prismatic granular sample, surrounded by a latex membrane, is placed between two fixed walls to create plane strain condition. Then the sample is subjected to axial loading, superimposed by a confining pressure applied on the membrane.

We are to discuss how the latex membrane can be modeled. One way would be to apply a perpendicular force on each edge of the polygons belonging to the external contour of the sample. This method works only in the case of dense polygonal samples. For loose samples the force will act on all the fjords of the boundary. This produces an uncontrollable growth of roughness of the boundary that with time, end up destroying the contact network of the sample. With a latex membrane this cannot happen because the bending stiffness of the membrane does not allow the pressure to penetrate in all the fjords of the sample. To model such a membrane, we will introduce a criterion which restricts the boundary points that are subjected to the external stress.

First we describe the method used to identify the boundary of the assembly. This boundary corresponds
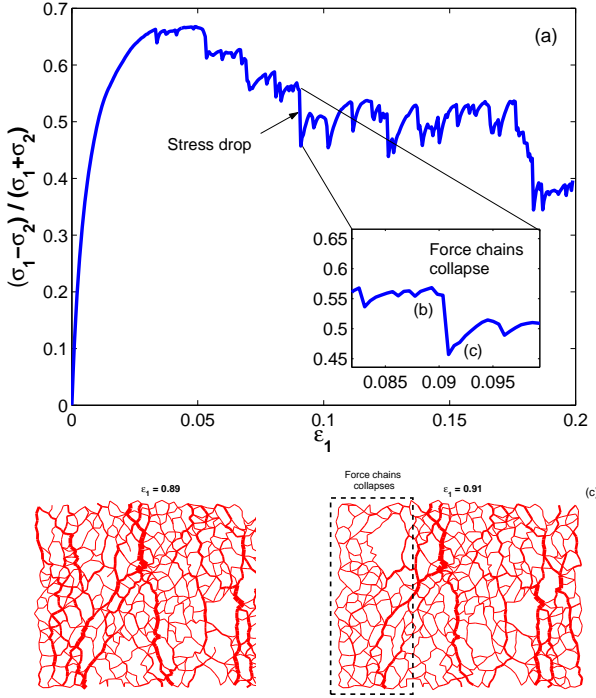
Fig. 3 Stress drops (a) and their correlation with collapse of force chains: force network just before the stress drop (b) and right after it (c). The width of the lines is proportional to the magnitude of the contact force. [17]

to a polygon, that is constructed as follows: The lowest vertex p from all the polygons of the sample is chosen as the first point of the boundary list b_1. In Fig. 4 P is the polygon that contains p, and $q \in P \cap Q$ is the first intersection point between the polygons P and Q in counterclockwise orientation with respect to p. Starting from p, the vertices of P in counterclockwise orientation are included in the boundary list until q is reached. Next, q is included in the boundary list. Then, the vertices of Q between q and the next intersection point $r \in Q \cap R$ in the counterclockwise orientation are included in the list. The same procedure is applied until one surrounds the sample and reaches the lowest vertex p again. This is a very fast algorithm, because it uses of the intersection points between the polygons, which are previously calculated to obtain the contact force in each time step.

The next step is to determine the points of the boundary which are in contact with the floppy boundary. Let's define $\{b_i\}$ the set of points of the boundary and $\{m_i\}$ the set of boundary points that are in contact with the membrane. They are selected using the following two stepsalgorithm: First, The set $\{m_i\}$ is initialized with the vertices of the smallest convex polygon that encloses the boundary (see Fig. 5). The lowest point of the boundary is selected as the first vertex of the polygon $m_1 = b_1$. The second one m_2 is the boundary point b_i that minimizes the angle $\angle(\overrightarrow{b_1 b_i})$ with respect to the horizontal.
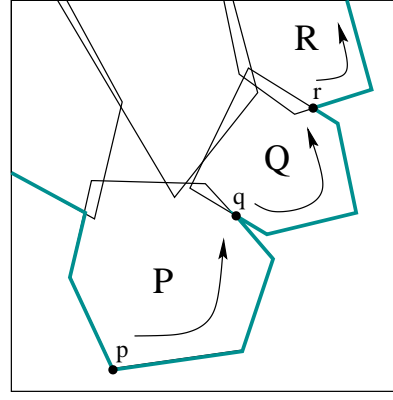

Fig. 4 Sketch of the algorithm used to find the boundary of the polygonal packing.

The third one m_3 is the boundary point b_i such that the angle $\angle(\overrightarrow{m_2 b_i}, \overrightarrow{m_1 m_2})$ is minimal. The algorithm is recursively applied until the lowest vertex m_1 is reached again. The final result is a convex polygon containning the sample, as shown part (a) of the Fig. 5.

In the second step of the algorithm, the points of the boundary are iteratively included in the list $\{m_i\}$ using the bending criterion proposed by Åstrøm [6]. For each pair of consecutive vertices of the membrane $m_i = b_i$ and $m_{i+1} = b_j$ we choose that point from the subset $\{b_k\}_{i \leq k \leq j}$ which maximizes the bending angle $\theta_b = \angle(\overrightarrow{b_k b_i}, \overrightarrow{b_k b_j})$. This point is included in the list whenever $\theta_b \geq \theta_{th}$. Here θ_{th} is a threshold angle for bending. This algorithm is repeatedly applied until there are no more points satisfying the bending condition. The final result gives a set of segments $\{\overline{m_i m_{i+1}}\}$ lying on the boundary of the sample as shown in Fig. 5.

In order to apply stress at the boundary, the segments of the membrane are divided into two groups: A-type segments are those that coincide with an edge of a boundary polygon; B-type segments connect the vertices of two different boundary polygons. On each segment of the membrane $\mathbf{T} = \Delta x_1 \hat{x}_1 + \Delta x_2 \hat{x}_2$, we apply a force

$$\mathbf{f}^b = -\sigma_1 \Delta x_2 \hat{x}_1 + \sigma_2 \Delta x_1 \hat{x}_2 \qquad (7)$$

Here $\hat{x}_1$ and $\hat{x}_2$ are the unit vectors of the Cartesian coordinate system. σ_1 and σ_2 are the components of the stress we want to apply on the sample. This force is transmitted to the polygons in contact with it. If the segment is A-type, this force is applied at its midpoint; if the segment is B-type, half of the force is applied at each one of the vertices connected by this segment. An additional damping force $\mathbf{f}_v^b = -\gamma_b m_i \mathbf{v}^\mathbf{b}$ is included to reduce the acoustic waves produced during loading. Here γ_b is the coefficient of viscosity of the floppy boundary, and m_i is the mass of the polygon and $\mathbf{v}^b$ the velocity of the polygon.

This boundary condition has been used in to simulate biaxial tests. First, a confining pressure is applied on the
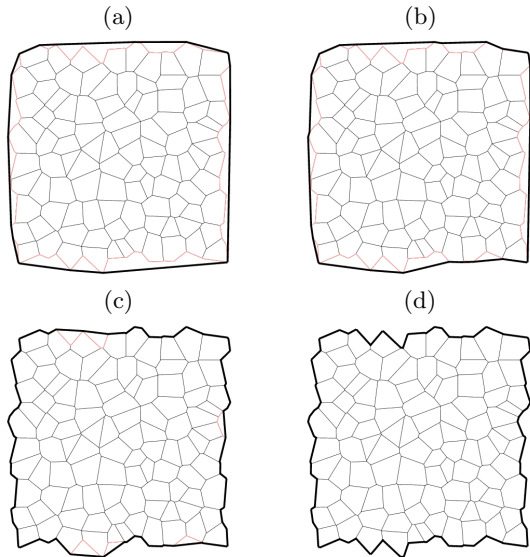
Fig. 5 Floppy boundary obtained with a maximal bending angle $\theta_{th} = \pi$, $3\pi/4$, $\pi/2$ and $\pi/4$, the first one corresponds to the minimum convex polygon that encloses the sample.

Fig. 6 Top left: Principal stress directions of the grains after failure ($\epsilon_1 = 0.07$); the confining pressure is $p_0 = 0.001k_n$. Top right: Detail of the stress in the shear band.

sample through the floppy boundary. Then two horizontal walls at the top and bottom of the packing are used to apply vertical loading with constant velocity. We have reproduced very clear shear bands whose orientation lies between the Mohr-Coulomb and Roscoe Solution, which defines with very good agreement the limit for the angles found in the experiments [13]. The characteristic width of the shear of the band can be associated to the propagation of stress inside the grains. The stress tensor at each particle P is given by $\sigma_{ij}^P = \frac{1}{a} \sum_c f_i^c \ell_j^c$ where a is the area of the polygon, f_i^c is the contact force and ℓ_j^c is the branch vector, connecting the center of mass of the polygon to the point of application of the contact force. The sum goes over all the contacts of the particle. The principal stress direction at each grain is represented in Fig. 6 by a cross. The length of the lines represents how large the components are. At the beginning of the loading, the major principal stress is almost parallel to the load direction, forming column-like structures which are called force chains. At failure these chains start buckling. The buckled chains gradually creates force loops which concentrate as shear bands. The size of such loops corresponds to the shear band width, and it depends mainly on the grain diameter. Buckling of each force chain involves rolling between the grains belonging to it, a feature that has been used to provide a theoretical explanation of the finite width of shear bands [25].

There are still some challenges in the modeling of such floppy boundary conditions: For small values of θ_{th} and loose samples the floppy boundary penetrates too much in the fjords, producing some instabilities in the boundary polygons. This instability is reflected in 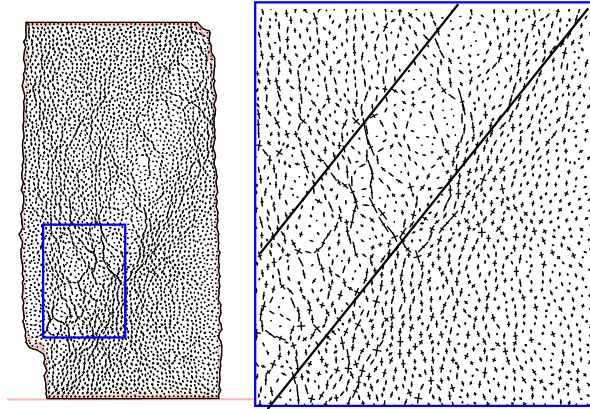large displacements on boundary polygons for small loadings, eventually leading to their detachment. For dense samples the method works fine, as it has proved in the calculation the incremental stress-strain relation of isolated representative element volumes [26].

Further complications of this method arise for values of θ_{th} close to π: When the sample is kept at constant isotropic pressure, the assembly cannot reach an equilibrium configuration. We have observed that in these cases the floppy boundary flips periodically to different configurations, giving rise to spurious oscillations in the assembly. A reason for this numerical problem could be the fact that this method leads to boundary forces which do not change continuously with time. In these cases, the numerical method used to solve the equations of motion cannot guarantee stability and convergence of the numerical solution.

5.3 Periodic Boundary Conditions

The periodic boundary technique is a very useful tool in granular dynamics simulations. The main feature is the ability to remove the surface effects, which are presented in any finite sample. It is also a way to make a simulation consisting of only a few hundred particles behave as if it was infinite in size.

We simulate extended shear zones using periodic boundary condition in the horizontal direction. The particles are contained in a space domain of length L. When a particle leaves the left (right) side of this domain, it reenters from the opposite site. In each time step, particles in the left (right) side of the domain can interact with the particles in the right (left) side. This is implemented by wrapping the link cell in Section 4 as a doughnut, so that particles in the left (right) cells of the link cell can be neighbor of the particles in the right (left) ones. If a pair of particles are neighbors through the periodic boundary condition, their interaction is calculated in three steps:

(1) shift the left particle by L; (2) calculate the contact force; and (3) shift the particle back.

Figure 7 shows four different stages of the shear band formation using periodic boundary conditions. The top and bottom layers of the sample have fixed boundary conditions. A constant confining normal force is imposed between these layer. The top and bottom layers are sheared in opposite direction with a fixed relative velocity v_x. The particles in these layers are not allowed to rotate or move against each other. To allow volumetric changes of the sample, the top boundary is free to move in vertical direction. A precursor of the shear band formation is the emergence of anisotropy of the contact network, as shown part (b) of the Figure 7. For large shear deformation shear bands of $6 - 8$ particle diameters arise for large shear deformation.

Shear cells with periodic boundary conditions has been used to investigate fault gouges [14; 27]. There is a growing interest in the investigation of the low dissipation on shear zones, which can potentially explain the long standing Heat Flow Paradox [18]. A detailed investigation of the transition from the stick to slip motion would also contribute to the understanding of earthquake nucleation. The time fluctuations in shear bands have also shown some similarities with the seismic activity in fault zones [7]. In should be however mentioned that the simulations of the acoustic emission after a collapse event does not behave similar to the elastic waves in real earthquakes. In the Earth seismic waves are able to travel through the plates. However, in the simulations accoustic waves are trapped by the periodic boundary condition and the reflective effect of the free boundaries. The development of transparent (or absorbing) boundary condition will be important to future application on seismic activity and wave propagation.

6 Concluding remarks

We presented a discrete model of polygonal particles to simulate shear bands. Under different boundary conditions, dense samples develop shear bands of $6 - 8$ particle diameters width. Loose samples do not show clearly shear bands. The dynamics of shear bands are characterized by building and collapse of force chains, which lead to stress fluctuations similar to the seismic activity in fault zones. There are several challenges in the modeling of more realistic fault zones:

(1) The interaction between polygons using the overlapping area is difficult to generalize in 3D, because the overlap between polyhedrons is much more difficult to evaluate.

(2) The elastic force used in this work does not belong from a potential, so that this model does not provide an equation for energy balance. In the investigation of fault zones, the energy balance is required to determine the energy budget in earthquakes.

(3) Earthquakes result from the combined effect of frictional instabilities and rock fragmentation. Thus, the modeling of realistic fault zones must include grain fragmentation.

To overcome the first two issues we are implementing a novel technique based on spherosimplexes [28]. This method provide an energy balance equations and a wide range of particle shape representations, including non-convex particles and tunable grain roundness. Inexpensive simulations of shear cells with grain crushing can be implemented by calculating the internal stress of the polygons in each time step, and imposing a stress threshold of breaking; When a polygon reaches this limit, it is then replaced by a set of smaller ones, having the same area as the original one. An important question is whether shear bands develop fractal distribution of grain sizes like in real fault gouges [1]. Understanding the dynamic of such fractal gouges will contribute to solve some enigmatic issues on earthquakes, such as the reason of the low heat production of fault zones and the origin of aseismic creep, where the two tectonic plates move each other without producing earthquake activity [29; 30].
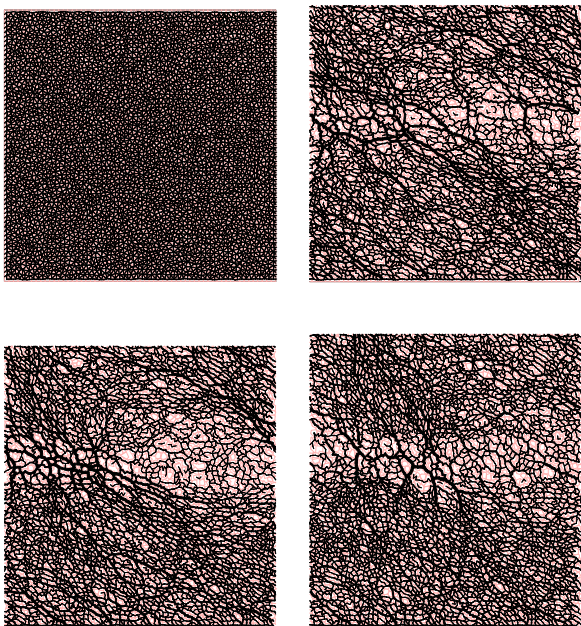

Fig. 7 Different stages of shear band formation using a polygonal packing with initially zero porosity. The lines represent the intensity of the normal force. Snapshots are taken for shear deformation of 0%, 0.05%, 0.1% and 0.2% the length of the sample.

and Instabilities in Geomaterials with Application to Hazard Mitigation (DIGA) in the framework of the Human Potential Program.

References

1. B Wilson, T Dewers, Z Reches, and J Brune. Particle size and energetics of gouge from earthquake rupture zones. *Nature*, 434:749 –752, 2005.

2. C. T. Veje, D. W. Howell, and R. P. Behringer. Kinematics of a two-dimensional granular couette experiment at the transition to shearing. *Phys. Rev. E*, 59(1):739–745, 1999.

3. T. Unger. Refraction of shear zones in granular materials. *Phys. Rev. Lett*, 98:018301, 2007.

4. J. Desrues and G. Viggiani. Strain localisation in sand. an overview of the experimental results obtained in grenoble using stereophotogrammetry. *Int. J. Numer. Anal. Meth. Geomech.*, 28:279–321, 2004.

5. M. Oda and K. Iwashita. Study on couple stress and shear band development in granular media based on numerical simulation analyses. *Int. J. of Enginering Science*, 38:1713–1740, 2000.

6. J. A. Astrom, H. J. Herrmann, and J. Timonen. Granular packings and fault zones. *Phys. Rev. Lett.*, 84:4638–4641, 2000.

7. P. Mora and D. Place. Simulation of the frictional stick-slip instability. *Pageoph.*, 143:61–87, 1994.

8. C. Moukarzel and H. J. Herrmann. A vectorizable random lattice. *Journal of Statistical Physics*, 68(5/6):911–923, 1992.

9. A. Okabe, B. Boots, and K. Sugihara. *Spatial Tessellations. Concepts and Applications of Voronoi Diagrams*. John Wiley & Sons, Chichester, 1992. Wiley Series in probability and Mathematical Statistics.

10. F. Alonso-Marroquin. *Micromechanical investigation of soil deformation: Incremental Response and granular Ratcheting*. PhD thesis, University of Stuttgart, 2004. Logos Verlag Berlin ISBN 3-8325-0560-1.

11. T. Marcher and P. A. Vermeer. Macromodelling of softening in non-cohesive soils. In *Continuous and Discontinuous Modelling of Cohesive Frictional Materials*, pages 89–110, Berlin, 2001. Springer.

12. J. Desrues. *Localisation de la deformation plastique dans les materieux granulaires*. PhD thesis, University of Grenoble, 1984.

13. F. Alonso-Marroquin, S. Luding, H.J. Herrmann, and I. Vardoulakis. Role of the anisotropy in the elastoplastic response of a polygonal packing. *Phys. Rev. E*, 51:051304, 2005.

14. H. J. Tillemans and H. J. Herrmann. Simulating deformations of granular solids under shear. *Physica A*, 217:261–288, 1995.

15. F. Kun and H. J. Herrmann. Transition from damage to fragmentation in collision of solids. *Phys. Rev. E*, 59(3):2623–2632, 1999.

16. P. A. Cundall and O. D. L. Strack. A discrete numerical model for granular assemblages. *Géotechnique*, 29:47–65, 1979.

17. A. Pena, A. Lizcano, F. Alonso-Marroquin, and H. J. Herrmann. Biaxial test simulations using a packing of polygonal particles. *Int. J. Numer. Anal. Meth. Geomech.*, 2007. Iny. J. Numer. Anal. Meth. Geomech.

18. F. Alonso-Marroqun, I. Vardoulakis, H. J. Herrmann, D. Weatherley, and P. Mora. Effect of rolling on dissipation in fault gouges. *Phys. Rev. E*, 74:031306, 2006.

19. F. Alonso-Marroquin and H. J. Herrmann. Ratcheting of granular materials. *Phys. Rev. Lett.*, 92(5):054301, 2004.

20. M. P. Allen and D. J. Tildesley. *Computer Simulation of Liquids*. Oxford University Press, Oxford, 1987.

21. T. Poeschel and T. Schwager. *Computational Granular dynamics*. Springer, Berlin, 2004.

22. S. Nasuno, A. Kudrolli, and J. P. Gollub. Friction in granular layers: Hysteresis and precursors. *Phys. Rev. Lett.*, 1997.

23. F. Adjemian amd P. Evesque and X. Jia. Ultrasonic experiment coupled with triaxial test for micro-seismicity detection in granular media. In R. García-Rojo, H.J. Herrmann, and S. McNamara, editors, *Powders and Grains 2005*, pages 281–285. Balkema, 2005.

24. I. Vardoulakis and I. O. Georgopoulos. The stress - dilatancy hypothesis revisited: shear - banding related instabilities. *Soils & Foundations*, 45:61–76, 2005.

25. M. Satake. Finite difference approach to the shear band formation from the viewpoint of particle column buckling. In *Thirteenth Sourtheast Asian Geotechical Conference*, pages 815–818, 1998.

26. F. Alonso-Marroquin and H. J. Herrmann. Calculation of the incremental stress-strain relation of a polygonal packing. *Phys. Rev. E*, 66:021301, 2002.

27. P. Mora and D. Place. The weakness of earthquake faults. *Geophys. Res. Lett.*, 26:123–126, 1999.

28. F. Alonso-Marroquin, S. Luding, and H. Muhlhaus. Effect of grain shape in the statistical mechanics of granular gases. in preparation.

29. P. Rosen, C. Werner, E. Fielding, S. Hensley, S. Buckley, and P. Vincent. Aseismic creep along the San Andres fault northwest of Parkfield, CA measured by radar interferometry. *Geophys. Res. Lett.*, 25:825–828, 1998.

30. A. H. Lachenbruch and J. H. Sass. Heat flow from cajon pass, fault strength, and tectonic implications. *J. Geophys. Res.*, 97(B4):4995–5015, 1992.